

Improving parameter estimation accuracy with torsion-bar antennasKazunari Eda,^{1,2,*} Ayaka Shoda,^{1,†} Yousuke Itoh,^{2,‡} and Masaki Ando^{1,2,3,§}¹*Department of Physics, Graduate School of Science, University of Tokyo, Tokyo 113-0033, Japan*²*Research center for the early universe (RESCEU), Graduate School of Science, University of Tokyo, Tokyo 113-0033, Japan*³*Gravitational Wave Project Office, Optical and Infrared Astronomy Division, National Astronomical Observatory, Osawa 2-21-1, Mitaka, Tokyo 181-8588, Japan*

(Received 4 July 2014; published 22 September 2014)

We propose a new antenna configuration of a torsion-bar antenna (TOBA) and study its performance. A TOBA is a novel type of an antenna for low-frequency gravitational waves (GWs) which consists of two bar-shaped orthogonal test masses. Previously only the rotation of the bars on the horizontal plane had been considered as an output signal. In this paper, we introduce a new antenna configuration for a TOBA to incorporate two additional outputs by measuring the rotation of the bars on the vertical planes. Such a triple-output TOBA can be regarded as a network of three coincident but misaligned interferometric detectors. The target sensitivity we consider in this paper is about $3 \times 10^{-20} \text{ Hz}^{-1/2}$ at 1 Hz. Since the triple-output TOBA is sensitive to all directions of GWs, event detection rates are improved by a factor of 1.7. It also increases the parameter resolution drastically for short-duration observations because the triple-output TOBA has three independent output signals and can discriminate two polarization modes of a short-duration GW signal even with single antenna. For instance, in the case of a 10^4 - 10^4 IMBH merger at 100 Mpc, the source location is typically measurable with an accuracy of ± 0.01 - 0.1 steradians which is roughly two order of magnitude better than the conventional single-output TOBA.

DOI: [10.1103/PhysRevD.90.064039](https://doi.org/10.1103/PhysRevD.90.064039)

PACS numbers: 04.30.-w, 04.80.-y

I. INTRODUCTION

A torsion-bar antenna (TOBA) is a gravitational-wave (GW) detector with two bar-shaped test masses which rotate differentially by the tidal force of GWs [1–4]. The main feature of the TOBA is that it has good sensitivity at low frequencies around 1 Hz even on the ground because of its low resonant frequency of the test masses in the rotational degrees of freedom. Other ground-based detectors such as LIGO [5], Virgo [6], and KAGRA [7] are sensitive to GWs only above about 10 Hz. The test masses of interferometers do not behave as free masses and the seismic noise is not reduced below 10 Hz since the resonant frequency of the pendulum mode is higher than that of torsional mode. Though space-borne GW detectors such as evolved Laser Interferometer Space Antenna [8] and DECihertz Interferometer Gravitational wave Observatory [9] are sensitive at low frequencies, such space missions need several decades to be launched. TOBA is the possible way to detect low-frequency GWs with less time and fewer costs on the ground.

The main observational targets of a TOBA are GWs from intermediate-mass black hole (IMBH) binaries. While numerous evidence for the existence of stellar mass BHs

and supermassive BHs has been obtained through electromagnetic observations, existence of IMBHs has yet to be confirmed clearly. Several candidates for IMBHs have been identified as ultraluminous X-ray sources [10–12] and as dynamics of globular clusters [13,14]. A detection of GWs from IMBHs would elucidate their existence and would measure their masses and their spin precisely [15]. Such information may provide clues to the dynamics and structure of globular clusters and to the evolution of supermassive BHs. However, because GW signals from IMBH binaries do not last long enough for us to use the Doppler modulation induced in the signal by the Earth's motion and because a conventional GW detector cannot break the degeneracy of two independent polarization modes of the GW for such short-duration signal, it is difficult to measure the waveform parameters and the direction of the source with a single detector. Precise estimation of the direction of the GW sources may enable us to perform complementary observations with electromagnetic waves which provide us more detailed information on IMBHs.

In this paper, we propose a new observational configuration for a TOBA to improve the measurement accuracies of waveform parameters and event detection rates. We can obtain three independent output signals by monitoring not only the horizontal rotation of the test masses, but also their vertical rotations. Since these three signals have different responses to GWs in such a way that they compensate for their insensitive directions to

* eda@resceu.s.u-tokyo.ac.jp† shoda@granite.phys.s.u-tokyo.ac.jp‡ yousuke_itoh@resceu.s.u-tokyo.ac.jp§ ando@phys.s.u-tokyo.ac.jp

GWs each other, the detection volume is enlarged and therefore event detection rates are improved. Furthermore, the waveform parameters can be determined with a single TOBA even though the observation time is shorter than a day. It will enable us to derive more information about GW sources with less detectors.

The rest of this paper is composed as follows. We present the details of our antenna configuration and the antenna pattern functions in Sec. II. In Sec. III, we show the accuracy of the parameter estimation evaluated by the Fisher analysis for both monochromatic sources and binary coalescences. Summary and conclusions are presented in Sec. IV.

II. NEW ANTENNA CONFIGURATION

A. Setup

A TOBA is a low-frequency GW antenna which consists of two orthogonal bar-shaped test masses. Each bar is supported at its center, and mirrors are attached to the both ends of each bar. When a GW passes through the antenna, the bars rotate differentially around z -axis as shown in Fig. 1. The GW signal is encoded in the angular motions which can be measured by the optical path difference in a laser interferometer as will be explained below. In the previous configuration, only the rotation angles on the xy plane, θ_1 and θ_2 had been considered as output signals [1]. In this paper, we develop the antenna configuration by considering the ϕ_1 and ϕ_2 degrees of freedom without changing the previous setup drastically.

In the presence of a GW signal h_{ij} , the bars are subjected to the tidal force of GWs and rotate differentially. They work as test masses for GW detection above the resonant frequency. The horizontal angular motion, θ_1 , of the test

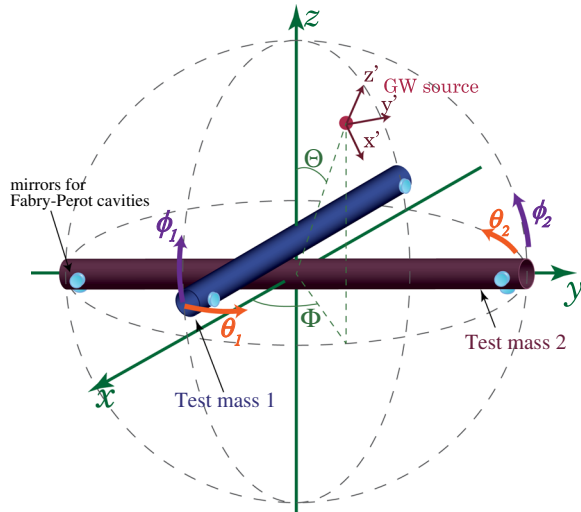


FIG. 1 (color online). Schematic picture of TOBA in the proper antenna frame. The test masses rotate in the horizontal plane (θ_1 and θ_2) and in the vertical planes (ϕ_1 and ϕ_2) due to the tidal force of GWs.

mass 1 from the original position obeys the equation of motion [1]:

$$I\ddot{\theta}_1(t) + \gamma_\theta\dot{\theta}_1(t) + \kappa_\theta\theta_1(t) = \frac{1}{4}\ddot{h}_{ij}q_{\theta_1}^{ij}, \quad (1)$$

where I , γ_θ , κ_θ , and $q_{\theta_1}^{ij}$ are the moment of inertia, dissipation coefficient and spring constant in the rotational degree of freedom, and the dynamic quadrupole moment of the horizontal rotational mode [16], respectively. We assume that each bar-shaped test mass is suspended by two wires at its center. The two test masses should be installed adjacent to each other as close as possible in order to reject the common-mode noise while they do not touch each other. As shown in Fig. 2, the test mass 1 has two holes at its center for the suspension wires of the test mass 2. This setup makes it possible for the centers of the two test masses to be positioned at the same point on the xy plane, so that the common-mode noise rejection is effective. Then, the spring constant κ_θ is derived by $\kappa_\theta = mga^2/l$, where g is the gravity acceleration, a is the distance between the two holes, and l is the length of the suspension wires. A TOBA is sensitive to GWs above the resonant frequency $f_\theta = \sqrt{\kappa_\theta/I}/2\pi$ for the θ degree of freedom. Figure 2 shows how to extract GW signals from angular motions of the bars. For instance, in the left panel in Fig. 2, an input laser beam is split into two orthogonal beams by a beam splitter, and after going back and forth in two Fabry-Perot cavities placed at the end of each bar the two beams are recombined at the beam splitter. Temporal change of difference in the cavity arm lengths due to the passage of a GW is measured by a photo-detector placed in the direction away from the laser which is not shown in Fig. 2.

Meanwhile, the angular motion in the vertical plane ϕ_1 obeys the equation of motion

$$I\ddot{\phi}_1(t) + \gamma_\phi\dot{\phi}_1(t) + \kappa_\phi\phi_1(t) = \frac{1}{4}\ddot{h}_{ij}q_{\phi_1}^{ij}. \quad (2)$$

The notation is basically the same as above. It means that the GW signals also appear in the rotation angle ϕ_1 . In this case, the spring constant for the ϕ degree of freedom κ_ϕ is written as

$$\kappa_\phi = mgd, \quad (3)$$

where d is the vertical distance between the center of mass of the test mass and the midpoint of the two suspension points. Therefore, the resonant frequency $f_{\phi_0} = \sqrt{\kappa_\phi/I}/2\pi$ will be below 10 mHz when the center of mass is adjusted so that $d \leq 3$ mm. The estimated sensitivity obtained by monitoring ϕ would be basically the same as θ except the suspension thermal noise when the configuration of the sensors are the same. The suspension thermal noise of the ϕ directions would be larger by a factor of $f_{\phi_0}/f_{\theta_0}\sqrt{Q_\theta/Q_\phi}$, where Q_i is the quality factor of the

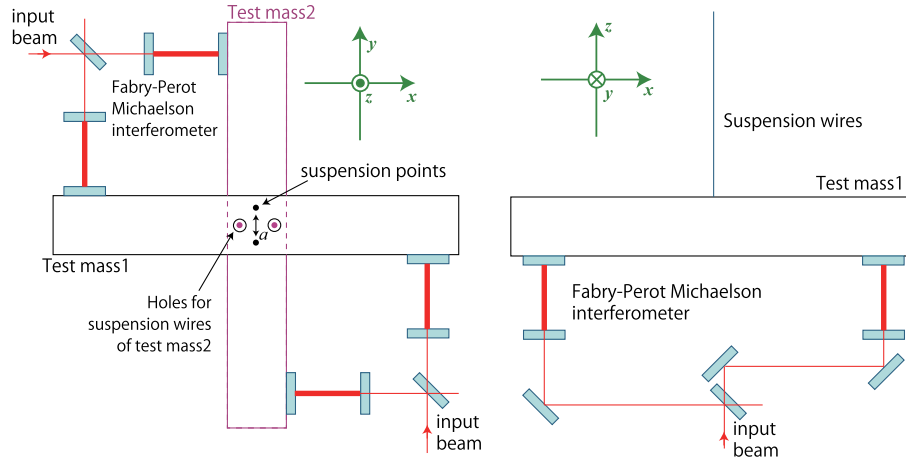


FIG. 2 (color online). This is the example of experimental configuration of two test masses. In the right panel, the test mass 2 is not shown for convenience. Each test mass is suspended by two wires. The test mass 1 has two holes with a distance a for the suspension wires of the test mass 2. The angular fluctuations of test masses are read by Fabry-Perot Michelson interferometers. Note that this setup is not fixed and should be discussed further in the process of the development.

fibers in the direction of i . However, the value of Q_ϕ is difficult to estimate theoretically and should be investigated experimentally because it is considered to largely depend on the suspension system such as wire clamps. Thus, we assume that the noise levels including the thermal noise for the θ and ϕ degrees of freedom are the same in this paper, so that the strain sensitivities involved with θ and ϕ are assumed to be the same.

The same equations of motion are applied to the test mass 2. Considering $\theta_2 = -\theta_1$ [1], we obtain three independent output signals, $s_I = \theta_1 - \theta_2$, $s_{II} = \phi_1$, and $s_{III} = \phi_2$. In the following, the output obtained from $\theta_1 - \theta_2$, ϕ_1 , and ϕ_2 are referred to as the output I, II, and III, respectively. The expected sensitivity curve for the output I with the parameters in Table I is represented in Fig. 3.

B. Antenna response

The response of the antenna to the incident GW depends on its relative position and orientation to the GW source. Such geometrical information is encoded in antenna pattern functions F_+ and F_\times which correspond to the two independent GW polarizations. Using F_+ and F_\times , the GW signal $h(t)$ in the antenna output is expressed by

$$h(t) = F_+(t)h_+(t) + F_\times(t)h_\times(t). \quad (4)$$

Let us introduce two coordinate systems, a proper antenna frame (x, y, z) such that the two bars are aligned with the x -axis and the y -axis as illustrated in Fig. 1 and a wave-coming frame (x', y', z') such that the direction of GW propagation is along the z' -axis. The GW waveform $\mathbf{h}(t)$ in the proper antenna frame can be related to the waveform $\mathbf{h}'(t)$ in the wave-coming frame by

$$\mathbf{h}(t) = M(t)\mathbf{h}'(t)M(t)^T \quad (5)$$

where M is the 3-dimensional transformation matrix and M^T denotes the transpose of the matrix M .

As discussed in the previous subsection, the two orthogonal bars are twisted differentially by the tidal force from the incoming GW. When the tidal force produces the small rotation of the bar on the x -axis toward the y -direction, the resulting GW signal is expressed by $h_{ij}n_x^i n_y^j$. Similarly, the GW signals h_I, h_{II} , and h_{III} of the three outputs obtained from $\theta_1 - \theta_2, \phi_1$ and ϕ_2 in Fig. 1 are expressed by

$$h_I = \frac{1}{2}(n_x^i n_y^j + n_y^i n_x^j)h_{ij} = n_x^i n_y^j h_{ij}, \quad (6a)$$

$$h_{II} = \frac{1}{2}n_x^i n_z^j h_{ij}, \quad (6b)$$

$$h_{III} = \frac{1}{2}n_y^i n_z^j h_{ij} \quad (6c)$$

where $\mathbf{n}_x, \mathbf{n}_y$, and \mathbf{n}_z are the unit vectors pointing toward the x, y and z -directions, respectively in the proper antenna frame. h_I, h_{II} , and h_{III} can be decomposed into the sum of the two independent polarization h_+ and h_\times as in Eq. (4). Combining Eqs. (5)–(6c), we can find the explicit expressions for the antenna pattern functions.

When the signal duration is so short that the relative motion of the antenna with respect to the sources is negligible, F_+ and F_\times can be regarded as constants. In this case, the pattern functions are given by

$$F_I^+ = -\frac{1 + \cos^2\Theta}{2} \sin 2\Phi \cos \Psi + \cos \Theta \cos 2\Phi \sin 2\Psi, \quad (7a)$$

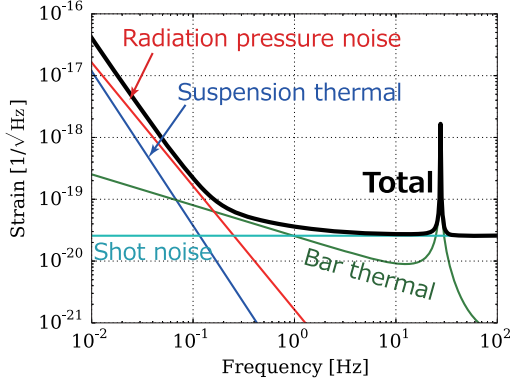


FIG. 3 (color online). The estimated sensitivity curve of 10-m scaled TOBA.

$$F_I^\times = \cos \Theta \cos 2\Phi \cos 2\Psi + \frac{1 + \cos^2 \Theta}{2} \sin 2\Phi \sin 2\Psi, \quad (7b)$$

$$F_{II}^+ = \frac{1}{4} \sin 2\Theta \sin \Phi \cos 2\Psi - \frac{1}{2} \sin \Theta \cos \Phi \sin 2\Psi, \quad (7c)$$

$$F_{II}^\times = -\frac{1}{2} \sin \Theta \cos \Phi \cos 2\Psi + \frac{1}{4} \sin 2\Theta \sin \Phi \sin 2\Psi, \quad (7d)$$

$$F_{III}^+ = \frac{1}{4} \sin 2\Theta \cos \Phi \cos 2\Psi + \frac{1}{2} \sin \Theta \sin \Phi \sin 2\Psi, \quad (7e)$$

$$F_{III}^\times = \frac{1}{2} \sin \Theta \sin \Phi \cos 2\Psi - \frac{1}{4} \sin 2\Theta \cos \Phi \sin 2\Psi \quad (7f)$$

where Ψ is the GW polarization angle. The direction of the incoming GW is assumed to be $\mathbf{n} = -(\sin \Theta \sin \Phi, \sin \Theta \cos \Phi, \cos \Theta)$ in the proper antenna frame. The antenna responses of the single-output TOBA shown in Eqs. (7a) and (7b) are basically equivalent to that of an interferometric detector.

For long-duration signals, the antenna and the source cannot be treated as at rest with respect to each other because of the Earth's rotation and revolution. So Θ and Φ in Eqs. (7a)–(7f) are not constant any longer. These relative motions induce the amplitude-modulation and phase-modulation of the signal. To take into account these effects, we follow the formulation presented by Jaranowski *et al.* [17,18] and obtain the following expressions for the antenna pattern functions.

$$F_N^+(t) = a_N(t) \cos 2\psi + b_N(t) \sin 2\psi, \quad (8a)$$

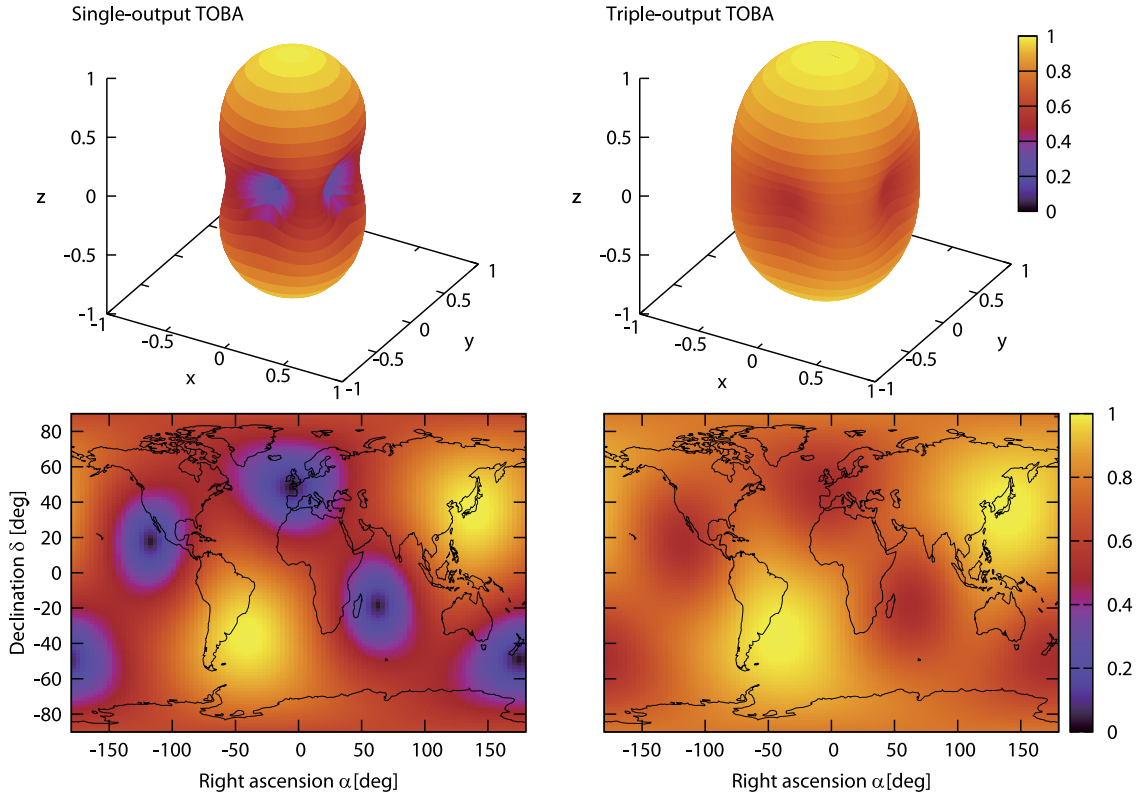


FIG. 4 (color online). Square root of the antenna power patterns $\sqrt{P_N}$ for the single-output TOBA (left panel) and the triple-output TOBA (right panel). The antennas are assumed to be located at the TAMA300's site in Japan ($35^\circ 40' 36''$ N, $139^\circ 32' 10''$ E).

$$F_N^\times(t) = b_N(t) \cos 2\psi - a_N(t) \sin 2\psi, \quad (8b)$$

$$N = \text{I, II, III.}$$

Explicit expressions for the modulation amplitudes $a_N(t)$ and $b_N(t)$ are given in Appendix A. The antenna pattern functions shown in Eqs. (8a), (8b), (A1a)–(A1f) contain the unknown parameters α, δ, ψ and the known parameters $\lambda, \gamma, \Omega_r, \phi_r$. The direction of the incident GW is specified by two parameters α and δ which are called right ascension and declination, respectively. The angle ψ denotes the GW polarization angle. The antenna on the Earth is located at the longitude λ and the latitude $\phi_r + \Omega_r t$ where Ω_r is the angular speed of the Earth and ϕ_r is the initial phase position. The antenna orientation γ is the angle between the local East direction and the bisector of the antenna.

C. Detection volume

The new configuration presented in subsection II A enhances the detection volume

$$V_N = \int d\Omega \int_0^{R_N(\alpha, \delta)} r^2 dr, \quad (9)$$

which represents the region enclosed by its reach in any direction [19] with

$$R_N(\alpha, \delta) = \frac{D}{\rho_{\min}} [P_N(\alpha, \delta)]^{1/2}. \quad (10)$$

Here D is the distance to which the antenna can observe GWs by a single signal with a unit signal-to-noise ratio (SNR), ρ_{\min} is the minimum value of the SNR above which we can regard that the GW signal is detected, and $P_N(\alpha, \delta) = \sum_N (F_N^{+2} + F_N^{\times 2})$ is the antenna pattern power function depicted in Fig. 4. In our case, the summation is taken over the three outputs I, II, and III. Figure 4 indicates that the triple-output TOBA has no blind direction and that its sensitivity is much more uniform than the conventional single-output TOBA.

When we take $\rho_{\min} = D = 1$ and assume that the sensitivity of the three signals are the same for convenience, then $V_1 = 1.2$ with the single signal, and $V_3 = 2.0$ with the three signals. When we obtain three signals with the same sensitivity, the detection volume will be about 1.7 times larger than the single output configuration.

III. PARAMETER RESOLUTION

In the following, we study how accurately we could measure the source location using a single and a network of triple-output TOBAs and also examine the measurement errors of the other waveform parameters. For this purpose we consider two nominal sources, monochromatic sources and IMBH binary coalescences. First, we examine the monochromatic source case for a fixed SNR in order to

reveal how the new configuration of the antenna improves the parameter resolution apart from the improved SNR. This examination gives an insight into the result of the IMBH mergers case. Then, we move on to discussions about IMBH mergers at a fixed distance, which are more realistic targets of a TOBA.

A. Fisher analysis

Before proceeding with calculations, we provide a brief review of the Fisher analysis to evaluate parameter estimation errors for a network of N_a antennas each of which has triple outputs (see [20–22] for more details). Each output $s_N(t)$ is assumed to be written as a sum of the noise $n_N(t)$ in the N th output and the GW signal $h_N(t)$, $s_N(t) = h_N(t) + n_N(t)$. If the noise is stationary, the correlation between the Fourier components of the noise can be expressed by

$$\langle \tilde{n}_N(f) \tilde{n}_M^*(f') \rangle = \frac{1}{2} \delta(f - f') S_n(f)_{NM} \quad (11)$$

where $\langle \dots \rangle$ denotes the ensemble average and $S_n(f)$ is a one-sided power spectral density matrix of the antenna network. It is convenient to introduce a noise-weighted inner product between two N_o -dimensional vector functions $\mathbf{f}(t)$ and $\mathbf{g}(t)$,

$$\langle \mathbf{f} | \mathbf{g} \rangle = 4 \text{Re} \sum_{N, M=1}^{N_o} \int_0^\infty df \frac{\tilde{f}_N(f) \tilde{g}_M^*(f)}{S_n(f)_{NM}} \quad (12)$$

where Re denotes the real part and N_o is the number of the total outputs of the network. Using this inner product, the SNR for the GW signal $\mathbf{h}(t)$ can be written as

$$\frac{S}{N} = (\mathbf{h} | \mathbf{h})^{1/2}. \quad (13)$$

We assume that the GW signal $h(t)$ is characterized by a collection of unknown parameters $\boldsymbol{\lambda} = \{\lambda_1, \dots, \lambda_n\}$. When the noise is Gaussian in addition to stationary, the statistical errors caused by the randomness of the antenna noises are estimated by

$$\langle \Delta \lambda^i \Delta \lambda^j \rangle = (\Gamma^{-1})_{ij} \quad (14)$$

for large S/N . The matrix Γ_{ij} is referred to as the Fisher information matrix defined by

$$\Gamma_{ij} = \left(\frac{\partial \mathbf{h}}{\partial \lambda^i} \middle| \frac{\partial \mathbf{h}}{\partial \lambda^j} \right). \quad (15)$$

To estimate the angular resolution of the antennas, we use the error in solid angle defined by

$$\Delta\Omega \equiv 2\pi|\sin\delta|\sqrt{\langle\Delta\alpha^2\rangle\langle\Delta\delta^2\rangle - \langle\Delta\alpha\Delta\delta\rangle^2}. \quad (16)$$

Throughout this paper, we assume that the noises of each output are uncorrelated with each other and that the form of their spectral densities are the same. In this case, the spectrum matrix $\mathbf{S}_n(f)$ has only diagonal elements all of which can be written with the same function $S_n(f)$.

In practice, it is necessary to reveal and solve some technical issues in actual antennas. For example, the loss angle of the suspension wire has to be investigated in the ϕ direction. Though we assumed that the sensitivities of all three signals are the same, the sensitivities should be different because of the suspension thermal noise in s_{II} and s_{III} which is considered to be larger than that in s_{I} as discussed in subsection II A.

Also, Newtonian noise would be one of the largest problems for low-frequency GW detection on the ground. Newtonian noise is the noise due to fluctuations in the local Newtonian gravitational field around the test masses which result from ambient density fluctuations in the ground and the atmosphere and from moving objects and humans near the test masses [23–25]. Newtonian noise has yet to be detected experimentally but would affect the sensitivity of a TOBA below $f = 0.1$ Hz [1]. We have to subtract the Newtonian noise, for example, using seismic sensor arrays to prevent the degradation of the SNR [26,27].

B. Monochromatic sources

1. GW waveform

We consider monochromatic GW with a frequency f_0 which can be written as

$$h_+(t) = A_+ \cos(2\pi f_0 t), \quad (17a)$$

$$\begin{aligned} \mathbf{n}_0 \cdot \mathbf{r}_d = R_{\text{ES}}[\cos\alpha \cos\delta \cos(\phi_o + \Omega_o t) + (\cos\varepsilon \sin\alpha \cos\delta + \sin\varepsilon \sin\delta) \sin(\phi_o + \Omega_o t)] \\ + R_{\text{E}}[\sin\lambda \sin\delta + \cos\lambda \cos\delta \cos(\alpha - \phi_r - \Omega_r t)] \end{aligned} \quad (20)$$

where R_{ES} is the distance between the SSB and the center of the Earth, R_{E} is the Earth's radius, Ω_o is the angular speed of the Earth's revolution around the Sun, ϕ_o is the initial phase which defines the Earth's position at $t = 0$ and ε is the Earth's axial tilt [18]. Here we neglect the Einstein time delay and the Shapiro time delay because these effects are unobservable at low-frequencies less than 1 Hz.

Combining Eqs. (4), (17a), (17b), and (19), we find the antenna response of the N th output to a monochromatic source as

$$h_N(t) = A_N(t) \cos[\Phi_N(t)] \quad (21)$$

$$h_\times(t) = A_\times \sin(2\pi f_0 t) \quad (17b)$$

where A_+ and A_\times are the amplitudes of the two independent polarizations. When the source is a Newtonian circular binary composed of two point masses, the amplitudes are given by

$$A_+ = \frac{4G\mu\omega_s R^2}{c^4 r} \frac{1 + \cos^2\iota}{2}, \quad (18a)$$

$$A_\times = \frac{4G\mu\omega_s R^2}{c^4 r} \cos\iota \quad (18b)$$

where ι , μ , R , ω_s and r is the inclination, the reduced mass, the orbital radius, the orbital frequency and the distance to the source, respectively (see e.g. [28]).

For monochromatic GW sources, the relative motion of the antenna with respect to them causes the Doppler shift which induces the time-dependence in the observed frequency. In order to correct the Doppler effect, we adopt the solar system barycenter (SSB) as the reference point where the time t is measured. The Doppler correction is given by the derivative of the Römer time delay which is defined as the delay between the arrival times of the antenna and the SSB;

$$\Delta t = \frac{\mathbf{n}_0 \cdot \mathbf{r}_d}{c} \quad (19)$$

where $\mathbf{r}_d(t)$ is the relative position vector pointing from the SSB to the antenna and \mathbf{n}_0 is the unit vector pointing from the SSB to the GW source. The inner product $\mathbf{r}_d \cdot \mathbf{n}_0$ is written as

where the suffix “ N ” stands for the N th output and the function $A_N(t)$, $Q_N(t)$, and $\Phi_N(t)$ are given as follows.

$$A_N(t) = \mathcal{A}Q_N(t), \quad (22a)$$

$$Q_N(t) = \left[\left(\frac{1 + \cos^2\iota}{2} \right)^2 F_N^{+2}(t) + \cos^2\iota F_N^{\times 2}(t) \right]^{1/2}, \quad (22b)$$

$$\Phi_N(t) = 2\pi f_0 t + \varphi_0 + \varphi_{p,N}(t) + \varphi_D(t), \quad (22c)$$

$$\varphi_{p,N}(t) = \arctan \left[-\frac{2 \cos\iota}{1 + \cos^2\iota} \frac{F_N^\times(t)}{F_N^+(t)} \right], \quad (22d)$$

$$\varphi_D(t) = 2\pi f_0 \frac{\mathbf{n}_0 \cdot \mathbf{r}_d(t)}{c} \quad (22e)$$

where \mathcal{A} is the overall amplitude and φ_0 is a constant reference phase. The phase shift $\varphi_D(t)$ which appears in the GW phase $\Phi(t)$ is called the Doppler phase because it comes from the Doppler correction (19). The phase shift $\varphi_{p,N}(t)$ is the polarization phase which depends on the angular pattern functions $F_+(t)$ and $F_\times(t)$.

2. Parameter resolution

The GW signal from the monochromatic source Eqs. (21)–(22e) is characterized by the seven waveform parameters, the overall amplitude, \mathcal{A} , the GW frequency, f_0 , the reference phase, φ_0 , the sky position of the source, α and δ , the polarization angle, ψ , the inclination, ι . Before proceeding we simplify the task of integration in the Fisher matrix (15). The time scale of change in $\Phi_N(t)$ is of the order of f_0 . Meanwhile, the temporal change in $A_N(t)$ is mainly caused by the Earth's rotation. So the amplitude $A_N(t)$ varies slowly with time in comparison with the phase $\Phi_N(t)$ and the inequality $f_0 \gg |dA_N/dt|/A_N$ holds. This leads to

$$\left(\frac{S}{N}\right)^2 \cong \frac{1}{S_n(f_0)} \sum_N \int_0^{T_{\text{obs}}} dt A_N(t)^2, \quad (23a)$$

$$\Gamma_{ij} \cong \frac{1}{S_n(f_0)} \sum_N \int_0^{T_{\text{obs}}} dt [\partial_i A_N(t) \partial_j A_N(t) + A_N(t)^2 \partial_i \Phi_N(t) \partial_j \Phi_N(t)] \quad (23b)$$

from Eqs. (13) and (15) where the rapidly oscillating terms in the integrand such as $\cos \Phi_N(t)$ and $\sin \Phi_N(t)$ are discarded and T_{obs} denotes the observation time [29,30]. Observing that $S_n(f_0)$ in Eq. (23b) can be eliminated by Eq. (23a), the measurement errors can be expressed in terms of S/N which is normalized by $S/N = 10$ in this section. Note that the measurement errors are independent of the form of $S_n(f)$. Making the substitution of Eqs. (22a)–(22e) into Eq. (23b) produces the values of the Fisher matrix elements Γ_{ij} . Using Eq. (14), we obtain the measurement errors.

Figure 5 shows the angular resolution for a monochromatic source with a frequency $f_0 = 1$ Hz using a single antenna located at the TAMA300's site in Japan. This result is normalized by $S/N = 10$ with parameters $\phi_r = \phi_o = 0$, $\alpha = \delta = \iota = \psi = 1.0$ radians. The two curves, the dashed line and the solid line correspond to the antennas which have one output and three outputs, respectively. As can be seen in Fig. 5, there is no difference between two curves for $T_{\text{obs}} > 1$ day because the angular resolution is mainly determined by the Doppler phase φ_D . When $T_{\text{obs}} > 1$ day, the error $\Delta\Omega$ drops with the observation time for $T_{\text{obs}} > 10^5$ seconds and approaches to the diffraction-limited accuracy [31]. This feature can be traced to the Doppler shift caused by the revolution around the Sun. The

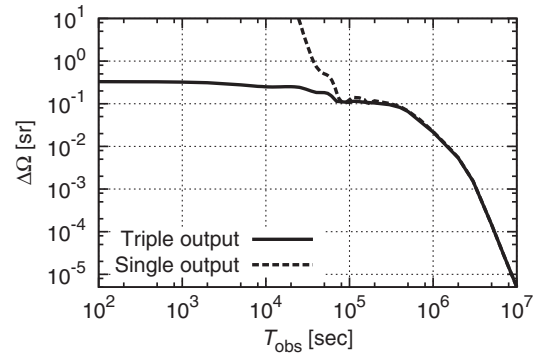


FIG. 5. Angular resolution $\Delta\Omega$ vs the observation time T_{obs} for monochromatic sources with $f_0 = 1$ Hz using a single antenna. We take the initial position and orientation of the antenna and the source position to be $\phi_r = \phi_o = 0$, $\alpha = \delta = \iota = \psi = 1.0$ radians. GW signals are normalized by $S/N = 10$. The solid line and the dashed line correspond to a triple-output TOBA and a one-output TOBA, respectively.

three-output antenna can be treated as the same way as the one-output antenna for such a long-duration signals with the fixed S/N . The difference between two curves appears in the short-duration signals such as $T_{\text{obs}} < 1$ day. The errors of the sky position for the one-output antenna decrease with time for $T_{\text{obs}} \gtrsim 10^4$ seconds due to the Doppler phase caused by the Earth's rotation. However, the one-output antenna cannot determine the source position for $T_{\text{obs}} \lesssim 10^4$ seconds at all. On the other hand, the angular resolution for the three-output antenna is of the order of 0.1 steradians and remains approximately constant regardless of the observation time less than 1 day. This feature can be traced to the polarization phase $\varphi_{p,N}$. For the three-output antenna, the two independent polarization modes, plus mode and cross mode can be discriminated because the three independent signals can be obtained even with a single antenna. The degeneracy of the two polarization modes is resolved by the

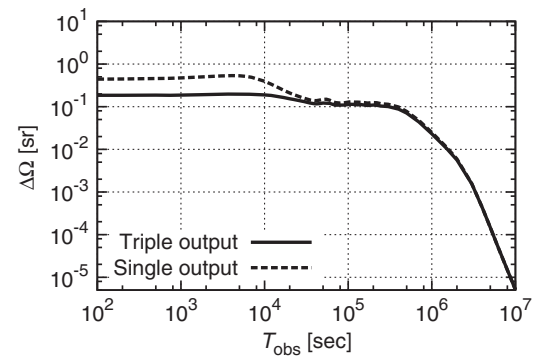


FIG. 6. Angular resolution $\Delta\Omega$ vs the observation time T_{obs} for monochromatic sources with $f_0 = 1$ Hz using three antennas. We take the initial position and orientation of the antenna and the source position to be $\phi_o = 0$, $\alpha = \delta = \iota = \psi = 1.0$ radians. GW signals are normalized by $S/N = 10$. The solid line and the dashed line correspond to a triple-output TOBA and a one-output TOBA, respectively.

TABLE I. Parameters of TOBA used for the estimated sensitivity curve shown in Fig. 3.

Test mass	Material	Aluminum
	Length of the bar	10 [m]
	Diameter of the bar	0.6 [m]
	Mass (m)	7400 [kg]
	Moment of inertia (I)	6.4×10^4 [N m s ²]
	Loss angle	10^{-7}
Suspension	Distance between the two suspension points (a)	5 [cm]
	Length of the suspension wires (l)	3 [m]
	Dissipation coefficient (γ_θ)	1.0×10^{-7}
Fabry-Perot laser interferometric sensor	Wave length	1064 [nm]
	Power	10 [W]
	Finesse	100

three-output antenna unlike the one-output antenna. Thus, the angular resolution of the three-output antenna for short-duration signals is much better than that of the one-output antenna thanks to the information on the polarization. Note that a mirror-image ambiguity remains in the location on the sky with a single antenna observation. Two or more antennas are required for resolving this ambiguity.

Figure 6 shows the angular resolution for the monochromatic source with the frequency $f_0 = 1.0$ Hz using a network of three antennas. This result is normalized by $S/N = 10$. Each antenna is located at the site of TAMA300 (Japan), LIGO-Hanford (US), and Virgo (Italy). The two curves, the dashed line and the solid line correspond to the antennas which have one output and three outputs, respectively. As can be seen in Fig. 6, the two curves coincide with each other for long-duration signals. This behavior is the same as the case for the observations with a single antenna for

$T_{\text{obs}} > 1$ day. On the other hand, the accuracy of the source location for a network of one-output antennas is constant and of the order of 0.1 steradians below $T_{\text{obs}} \sim 10^4$ seconds because it is mainly determined by the polarization phase $\varphi_{p,N}$. It should be noted that the angular resolution of a network of ground-based laser interferometers which are sensitive to an audio frequency signal is determined by the error of the delays of the arrival time [32]. It is roughly estimated by the geometrical formula derived by Wen and Chen [33]

$$\Delta\Omega = 0.25 \left(\frac{10 \text{ Hz}}{f_0} \right)^2 \left(\frac{3 \times 10^{13} \text{ m}^2}{A} \right) \left(\frac{0.5}{\cos\chi} \right) \left(\frac{10}{S/N} \right)^2 \times \left(\frac{(S/N)_1(S/N)_2(S/N)_3}{3\sqrt{3}(S/N)^3} \right)^{-1} \quad (24)$$

TABLE II. Angular resolution for monochromatic sources with frequency f_0 using the single triple-output TOBA for 1-hour observation. The result is normalized by $S/N = 10$. $(S/N)_I$ denotes the SNR of the output I. We take the value of the initial position and orientation of the antenna to be $\phi_r = \phi_o = 0$ radians.

f_0 [Hz]	α [rad]	δ [rad]	ι [rad]	ψ [rad]	\mathcal{A}	$(S/N)_I$	$\Delta\Omega$ [sr]
1.0	1.0	1.0	0.45	1.0	7.60×10^{-21}	8.90	0.332
	0.5	-1.0	0.45	0.0	9.76×10^{-21}	6.82	0.184
	1.0	1.0	1.0	1.0	1.24×10^{-20}	8.73	0.292
	0.5	-1.0	1.0	0.0	1.45×10^{-20}	7.07	0.187
	1.0	1.0	1.5	1.0	3.69×10^{-20}	4.82	0.206
	0.5	-1.0	1.5	0.0	2.43×10^{-20}	8.09	0.365
0.1	1.0	1.0	0.45	1.0	3.87×10^{-20}	8.90	0.332
	0.5	-1.0	0.45	0.0	4.97×10^{-20}	6.82	0.184
	1.0	1.0	1.0	1.0	6.29×10^{-20}	8.73	0.292
	0.5	-1.0	1.0	0.0	7.52×10^{-20}	7.07	0.187
	1.0	1.0	1.5	1.0	1.88×10^{-19}	4.82	0.206
	0.5	-1.0	1.5	0.0	1.24×10^{-19}	8.09	0.365
0.01	1.0	1.0	0.45	1.0	3.44×10^{-18}	8.90	0.332
	0.5	-1.0	0.45	0.0	4.42×10^{-18}	6.82	0.184
	1.0	1.0	1.0	1.0	5.60×10^{-18}	8.73	0.292
	0.5	-1.0	1.0	0.0	6.67×10^{-18}	7.07	0.187
	1.0	1.0	1.5	1.0	1.67×10^{-17}	4.82	0.206
	0.5	-1.0	1.5	0.0	1.10×10^{-17}	8.09	0.365

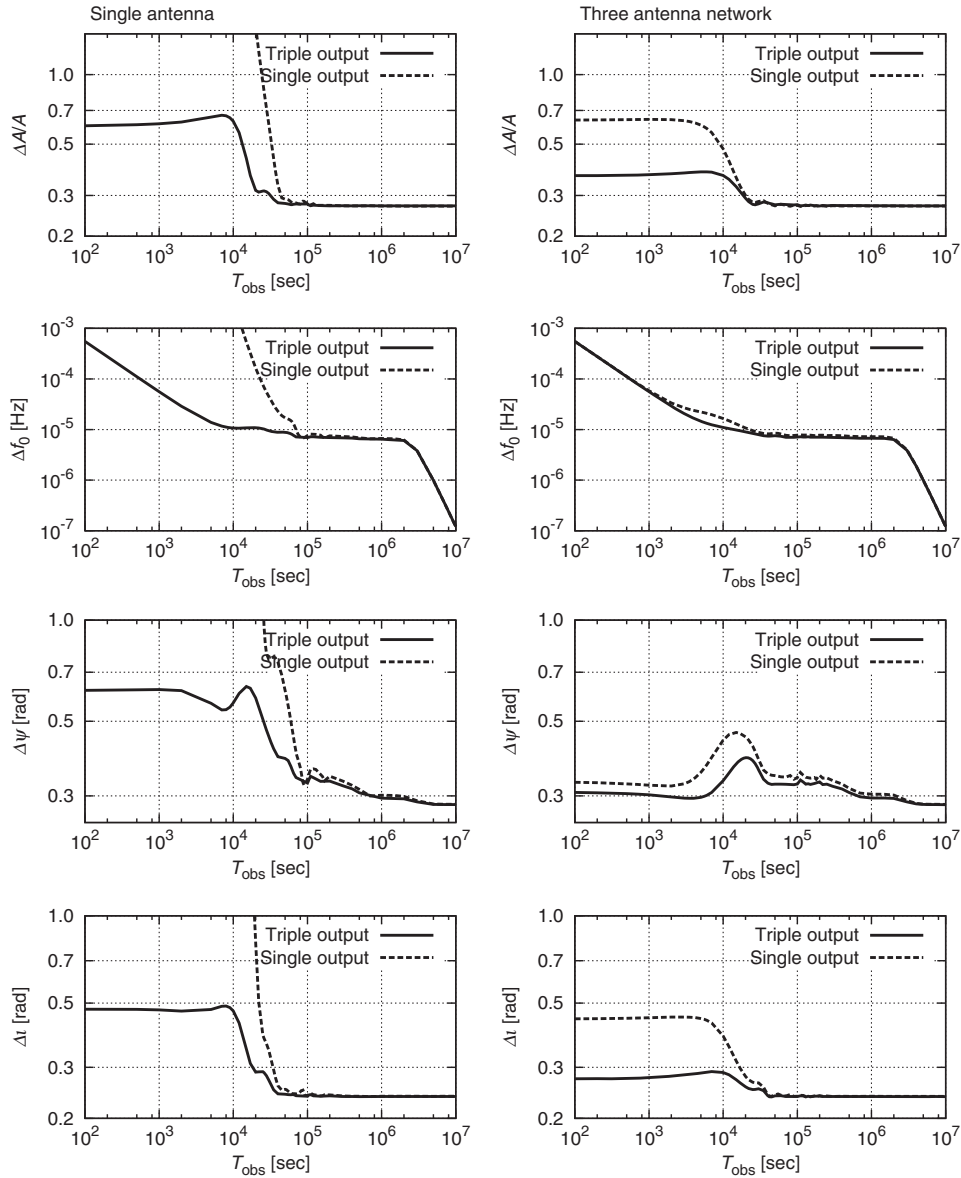


FIG. 7. Parameter accuracies for the monochromatic source with frequency $f_0 = 1$ Hz are plotted vs observation time T_{obs} . The left and right column correspond to a single antenna case and a three antenna network case, respectively. All results are normalized by $S/N = 10$. The initial position and orientation of the antenna at the TAMA300's site and the angular parameters are assumed to be $\phi_r = \phi_o = 0$, $\alpha = \delta = \iota = \psi = 1.0$.

where f_0 is the GW frequency, A is the area formed by the network of the three antennas, S/N is the total SNR, $(S/N)_i$ is the SNR achievable with the i th antenna alone, and χ is the angle between the normal to the plane defined by the antennas and the direction of GW propagation. The value $3 \times 10^{13} \text{ m}^2$ corresponds to the area formed by the TAMA-LIGO-Virgo network. This formula proportional to $1/f_0^2$ does not work when applied to a low frequency source because the directional derivatives of the pattern functions such as $\partial F_+/\partial \alpha$ are neglected in the derivation of Eq. (24) [33]. When the source location is identified using the network of the TOBAs which are sensitive to a sub-audio frequency signal, the polarization phases $\varphi_{p,N}$ but not the

Doppler phase φ_D play a key role in its angular resolution. The difference between two curves in Fig. 6 comes from the number of the independent outputs in each antenna.

Table II lists the angular resolution for the various frequencies and angular parameters. The results in Table II indicates the angular resolution for short-duration signals is independent of the GW frequency f_0 because it is determined by $\varphi_{p,N}(t)$ which does not depend on f_0 .

The measurement errors of the other waveform parameters ΔA , Δf_0 , $\Delta \psi$ and $\Delta \iota$ for the monochromatic wave with $f_0 = 1$ Hz are described in Fig. 7. These results are also normalized by $S/N = 10$. The behavior of the curves in Fig. 7 can essentially be explained in the same way as we

TABLE III. Angular resolution for IMBH-IMBH binary coalescence signals from a distance of 100 Mpc using the single antenna on the TAMA300's site. $(S/N)_I$ denotes the SNR of the output I defined by (6a). S/N denotes the total SNR of the single antenna.

m_1 [M_\odot]	m_2 [M_\odot]	α [rad]	δ [rad]	ι [rad]	ψ [rad]	$(S/N)_I$	S/N	$\Delta\Omega_I$ [sr]	$\Delta\Omega$ [sr]	$\Delta \ln \mathcal{A}_I$	$\Delta \ln \mathcal{A}$	Δt_I [rad]	Δt [rad]	$\Delta\psi_I$ [rad]	$\Delta\psi$ [rad]
10 ⁴	10 ⁴	1.0	1.0	1.0	1.0	29.9	35.3	4.02	0.0253	1.76	0.165	0.976	0.132	1.67	0.172
		2.0	-1.0	0.5	3.0	46.1	54.3	2.70	0.0207	3.75	0.631	7.44	1.25	0.833	2.60
		1.0	-1.5	0.5	4.0	40.1	50.6	23.2	0.258	3.97	0.697	8.05	1.38	13.6	2.38
		-3.0	0.5	1.0	0.0	25.0	32.2	0.765	0.0265	2.17	0.246	1.92	0.178	2.16	0.198
		3.0	1.5	1.0	2.0	23.4	31.9	47.2	0.348	1.40	0.166	1.00	0.143	12.3	1.11
		-1.0	1.0	0.5	6.0	48.6	55.8	2.90	0.0188	3.94	0.652	7.60	1.23	13.4	2.52
		-2.0	-0.5	1.0	5.0	26.8	34.4	1.47	0.0757	2.13	0.261	1.39	0.252	1.39	0.409
		All-sky average	1.0	1.0	1.0	25.9	33.2	6.82	0.0674	1.46	0.216	1.30	0.181	2.61	0.285
10 ⁴	10 ⁵	1.0	1.0	1.0	1.0	10.3	12.3	4.18	0.180	1.80	0.414	1.04	0.339	1.67	0.448
		2.0	-1.0	0.5	3.0	16.4	19.2	2.93	0.127	3.79	1.54	7.49	3.03	14.4	6.36
		1.0	-1.5	0.5	4.0	14.1	17.8	24.8	1.58	4.08	1.70	8.24	3.38	14.2	5.69
		-3.0	0.5	1.0	0.0	8.77	11.4	0.846	0.170	2.30	0.566	2.04	0.424	2.18	0.518
		3.0	1.5	1.0	2.0	8.21	11.2	49.9	2.35	1.47	0.444	1.08	0.370	12.4	2.78
		-1.0	1.0	0.5	6.0	17.3	19.7	3.12	0.120	4.10	1.61	7.92	3.05	13.8	6.28
		-2.0	-0.5	1.0	5.0	9.11	11.9	1.58	0.311	2.32	0.551	1.52	0.519	1.49	0.790
		All-sky average	1.0	1.0	1.0	9.12	11.7	7.26	0.383	1.54	0.490	1.37	0.416	2.73	0.673
10 ⁵	10 ⁵	1.0	1.0	1.0	1.0	13.4	16.0	4.11	0.113	1.75	0.336	1.00	0.273	0.448	0.358
		2.0	-1.0	0.5	3.0	21.1	24.8	2.82	0.0841	3.72	1.26	7.35	2.49	6.36	5.21
		1.0	-1.5	0.5	4.0	18.2	23.0	24.2	1.05	3.97	1.40	8.02	2.77	5.69	4.70
		-3.0	0.5	1.0	0.0	11.3	14.7	0.804	0.112	2.28	0.475	2.02	0.352	0.518	0.415
		3.0	1.5	1.0	2.0	10.6	14.4	48.1	1.51	1.39	0.352	1.03	0.297	2.78	2.26
		-1.0	1.0	0.5	6.0	22.2	25.4	2.99	0.0785	3.91	1.32	7.57	2.48	6.28	5.11
		-2.0	-0.5	1.0	5.0	11.9	15.5	1.55	0.238	2.19	0.475	1.43	0.451	0.790	0.703
		All-sky average	1.0	1.0	1.0	11.8	15.1	7.05	0.258	1.50	0.406	1.34	0.344	2.68	0.553

discussed above. For short-duration signals with the observation time less than 10^4 seconds, the errors are determined by the polarization phase $\varphi_{p,N}$ for both a single and a network of triple-output antennas. When $T_{\text{obs}} > 10^4$ seconds oscillating parts appear in Fig. 7 due to the phase-modulation induced by the Earth's spin. The triple outputs improve the parameter accuracies of the short-duration signals drastically for the single antenna case and improve them by several factors for the three antenna network case.

C. IMBH-IMBH binary coalescence

1. GW waveform

In this section, we consider a coalescing binary system composed of two point masses with m_1 and m_2 as a GW source. Unlike the monochromatic sources we discussed in the previous section, the orbital radius shrinks with time and the orbital frequency increases accordingly because of the GW radiation. In this case, the parameter accuracies depend on the form of the noise spectral density of the antenna $S_n(f)$. As a signal model from the binary coalescing, we adopt the restricted post-Newtonian waveform with the 1.5 PN phase in which the amplitude is retained up to the Newtonian order:

$$\tilde{h}_N(f) = \mathcal{A} Q_N(t_*) f^{-7/6} e^{-i(\varphi_{p,N}(t_*) + \varphi_D(t_*))} e^{i\Psi(f)}, \quad (25a)$$

$$\mathcal{A} \equiv \sqrt{\frac{5}{24}} \frac{1}{\pi^{2/3}} \frac{c}{r} \left(\frac{GM_c}{c^3} \right)^{5/6}, \quad (25b)$$

$$\Psi(f) = 2\pi f t_c - \frac{\pi}{4} - \phi_c - \tilde{\Phi}(f), \quad (25c)$$

$$\begin{aligned} \tilde{\Phi}(f) &= -\frac{3}{4} \left(\frac{GM_c}{c^3} 8\pi f \right)^{-5/3} \\ &\times \left[1 + \frac{20}{9} \left(\frac{743}{336} + \frac{11}{4} \eta \right) x - 16\pi x^{3/2} \right], \end{aligned} \quad (25d)$$

$$\begin{aligned} t_*(f) &= t_c - 5 \left(\frac{GM_c}{c^3} \right)^{-5/3} (8\pi f)^{-8/3} \\ &\times \left[1 + \frac{4}{3} \left(\frac{743}{336} + \frac{11}{4} \eta \right) x - \frac{32}{5} \pi x^{3/2} \right] \end{aligned} \quad (25e)$$

where r , t_c , and ϕ_c are the distance to the source, the time and the phase at the coalescence, respectively (see e.g. [28]). The mass $M_c \equiv (m_1 m_2)^{3/5} (m_1 + m_2)^{-1/5}$ and the mass ratio $\eta \equiv m_1 m_2 / (m_1 + m_2)^2$ are called a chirp mass and a symmetric mass ratio respectively, and a PN variable

TABLE IV. Angular resolution for IMBH-IMBH binary coalescence signals from a distance of 100 Mpc using the network of three antennas located on the site of TAMA300, LIGO-Hanford, and Virgo. $(S/N)_1$ denotes the total SNR of the network of the three antenna each of which has the only output I. S/N denotes the total SNR of the three antenna network.

m_1 [M_\odot]	m_2 [M_\odot]	α [rad]	δ [rad]	ι [rad]	ψ [rad]	$(S/N)_1$	S/N	$\Delta\Omega_1$ [sr]	$\Delta\Omega$ [sr]	$\Delta \ln \mathcal{A}_1$	$\Delta \ln \mathcal{A}$	Δt_1 [rad]	Δt [rad]	$\Delta\psi_1$ [rad]	$\Delta\psi$ [rad]
10 ⁴	10 ⁴	1.0	1.0	1.0	1.0	48.5	59.2	0.0165	0.00514	0.122	0.0613	0.0852	0.0460	0.696	0.0524
		2.0	-1.0	0.5	3.0	76.7	89.9	0.00404	0.00187	0.399	0.270	0.777	0.524	1.64	1.10
		1.0	-1.5	0.5	4.0	78.5	93.0	0.0373	0.0212	0.305	0.204	0.578	0.401	1.24	0.819
		-3.0	0.5	1.0	0.0	47.9	59.9	0.00232	0.00181	0.0639	0.0514	0.0579	0.0467	0.0729	0.0610
		3.0	1.5	1.0	2.0	54.3	64.1	0.0831	0.0440	0.0716	0.0500	0.0767	0.0511	0.462	0.336
		-1.0	1.0	0.5	6.0	77.3	90.5	0.00536	0.00209	0.426	0.267	0.797	0.502	1.65	1.04
		-2.0	-0.5	1.0	5.0	44.3	56.9	0.00456	0.00210	0.114	0.0653	0.0891	0.0520	0.129	0.0724
		All-sky average	1.0	1.0	1.0	49.1	59.3	0.0248	0.00744	0.131	0.0645	0.114	0.0555	0.177	0.0931
10 ⁴	10 ⁵	1.0	1.0	1.0	1.0	17.0	20.8	0.106	0.0393	0.311	0.170	0.219	0.128	0.201	0.153
		2.0	-1.0	0.5	3.0	27.0	31.6	0.0302	0.0146	1.05	0.734	2.04	1.42	4.21	2.93
		1.0	-1.5	0.5	4.0	27.5	32.6	0.276	0.166	0.824	0.584	1.56	1.11	3.24	2.21
		-3.0	0.5	1.0	0.0	16.8	21.0	0.0203	0.0155	0.182	0.147	0.165	0.134	0.211	0.177
		3.0	1.5	1.0	2.0	19.1	22.5	0.601	0.343	0.192	0.139	0.208	0.143	1.24	0.935
		-1.0	1.0	0.5	6.0	27.2	31.8	0.0386	0.0163	1.08	0.711	2.03	1.35	4.26	2.81
		-2.0	-0.5	1.0	5.0	15.6	20.0	0.0366	0.0172	0.307	0.181	0.242	0.145	0.337	0.201
		All-sky average	1.0	1.0	1.0	17.2	20.8	0.133	0.0571	0.305	0.178	0.267	0.153	0.425	0.258
10 ⁵	10 ⁵	1.0	1.0	1.0	1.0	22.0	26.9	0.0691	0.0241	0.250	0.133	0.76	0.100	0.155	0.117
		2.0	-1.0	0.5	3.0	34.9	40.8	0.0187	0.00890	0.840	0.579	1.63	1.12	3.39	2.33
		1.0	-1.5	0.5	4.0	35.6	42.1	0.171	0.101	0.652	0.456	1.24	0.870	2.58	1.74
		-3.0	0.5	1.0	0.0	21.7	27.2	0.0119	0.00912	0.141	0.114	0.127	0.103	0.162	0.136
		3.0	1.5	1.0	2.0	24.7	29.1	0.376	0.209	0.152	0.109	0.164	0.111	0.979	0.730
		-1.0	1.0	0.5	6.0	35.1	41.1	0.0242	0.00991	0.875	0.515	1.64	1.07	3.41	2.21
		-2.0	-0.5	1.0	5.0	20.1	25.8	0.0221	0.00103	0.243	0.142	0.191	0.113	0.270	0.157
		All-sky average	1.0	1.0	1.0	22.3	26.9	0.0890	0.0350	0.251	0.139	0.220	0.120	0.347	0.202

$x \equiv [\pi G(m_1 + m_2)f/c^3]^{2/3}$ was introduced. We cut off the GW signal at $f_{\max} \equiv c^3/6\sqrt{6}\pi G(m_1 + m_2)$ beyond which the circular orbit is not stable any longer and the two point masses plunge toward each other. So we set $\hat{h}(f) = 0$ for $f > f_{\max}$ in Eq. (25a).

2. Parameter resolution

We analyze the angular resolution for the coalescing IMBH binary signal using Eqs. (25a)–(25e). The GW signal is described by eight waveform parameters, the overall amplitude, \mathcal{A} , the coalescence time, t_c , the coalescence phase, ϕ_c , the sky position of the source, α and δ , the polarization angle, ψ , the inclination, ι , and the chirp mass, M_c . Substitution of Eq. (25a) into Eq. (15) yields the values of Fisher matrix elements. From Eq. (14) we get the accuracies of the waveform parameters.

We present a representative examples of our result in Table III and IV where source parameters are chosen randomly. We set the coalescence binary at 100 Mpc and the initial position of the antenna located at the TAMA300's site to be $\phi_r = \phi_o = 0$. Here, we do not assume the fixed SNR and neglect the effect of the expansion of the Universe and the higher order terms in the post-Newtonian expansion. However, the angular

resolution $\Delta\Omega$ we calculate in this paper is expected to be accurate because the angular resolution is accumulated at the inspiral phase long before the final plunge.

The S/N and the angular resolution $\Delta\Omega$ for the single antenna case (the three antenna network case) are listed in Table III (Table IV). The result of the single antenna case listed in Table III shows that the triple-output antenna improves the S/N by a factor of about 1.2 in comparison with the one-output antenna. The same can be said of the three antenna network listed in Table IV. This factor can be simply explained by $\sqrt{1^2 + (1/2)^2 + (1/2)^2} \cong 1.22$ from Eqs. (6a)–(6c). As can be seen in Table III, the angular resolution of the single three-output antenna $\Delta\Omega$ ranges from 10^{-2} to 1 steradians. It is roughly an order of magnitude better than that of the one-output antenna. This is because the angular resolution for short-duration signals such as signals from coalescing binaries is mainly determined by the polarization phase $\varphi_{p,N}(t)$ but not the Doppler phase $\varphi_D(t)$ as we discussed in the previous section where the monochromatic source was investigated. Since the two polarization modes (plus and cross modes) are degenerate in the single antenna which has the only one output, it is hard to locate the GW sources for short-duration signals. However, the single three-output antenna

can identify the source location to some degree because the degeneracy of the two polarization modes is resolved. Table IV shows that the angular resolution of the network of three-output antennas ranges roughly from 0.1 to 10^{-3} steradians. It is a factor of about 2 better than that of the one-output antenna network. This improvement is accomplished mainly by increasing S/N which comes from the triple outputs. The measurement errors of the other waveform parameters such as $\Delta\mathcal{A}/\mathcal{A}$ are also improved by several factors due to the additional outputs.

IV. CONCLUSION

In this paper we have presented a new GW antenna configuration with a triple-output TOBA and investigated its performance. Previously a single-output TOBA which monitors the angular motions caused by GWs only on the horizontal plane had been presented. We have developed the antenna configuration by adding two other outputs which are given by the angular motions on the vertical planes. Thus the gravitational wave signals can be readout from the small rotation of the bars on the x - y , y - z , and z - x planes as can be seen in Fig. 1.

We derive the antenna pattern functions of the triple-output TOBA including the effect of the Earth's motion and obtain Eqs. (8a) and (8b). The antenna pattern power is depicted in Fig. 4, which shows the triple-output TOBA has no blind direction and is sensitive to GWs from all directions. Its detection event rates is better than the single-output configuration by a factor of about 1.7.

We also analyze the accuracies of waveform parameters, focusing on the accuracy of the source location on the sky, for the two nominal sources, monochromatic sources and binary coalescences. For long-duration signals, the triple-output TOBA can be treated as the same way as the conventional single-output TOBA apart from the improved SNR, as expected. So the advantage of the triple outputs is merely the accumulation of the SNR. On the other hand, since the triple-output TOBA can break the degeneracy of two polarization modes from short-duration signals even with a single antenna, it improves the parameter estimation errors drastically compared with the single-output TOBA.

Thus, the detection method using a triple-output TOBA we proposed would be a powerful tool to search for short-duration signals such as a coalescing binary.

For future work, it would be interesting to investigate the potential of triple-output TOBAs for testing gravitational theories with GWs. Generally, alternative theories of gravity allow GWs to have more independent polarization modes up to six [34]. While several conventional interferometric detectors are required to separate a mixture of polarization modes of a GW in detector outputs, triple-output TOBAs may be able to put constraints on the nontensorial modes with less antennas because three independent signals can be extracted from each TOBA.

In addition, this work is considered to be applicable not only for the GW detection but also for a prompt earthquake detection [35]. Current earthquake early warning systems (EWS) make use of a seismic pressure wave, called a P-wave, caused by an earthquake which travels within the Earth with a velocity of a few km/s. Gravity perturbations are also induced by the earthquake during the fault rupture and propagate at the speed of light 3×10^5 km/s. Such gravity signals can be detected by a TOBA before the arrival of the seismic motion at the EWS. Therefore, a network of triple-output TOBAs would enable us to locate the origin of the earthquake and to estimate the earthquake intensity much earlier than the conventional EWS.

ACKNOWLEDGMENTS

We thank Jun'ichi Yokoyama for fruitful discussions. One of the authors (K. E.) also thanks Hiroataka Yuzurihara for helpful comments. This work is supported by Grant-in-Aid for JSPS Fellows Nos. 26.8636 (KE) and 24.7531 (AS), and Grant-in-Aid for Scientific Research No. 24244031 (MA).

APPENDIX: MODULATION AMPLITUDES

In this appendix, we give the explicit expressions for the modulation amplitudes which appear in Eqs. (8a) and (8b) as follows.

$$\begin{aligned}
 a_1(t) = & \frac{3}{4} \cos 2\gamma \cos^2 \delta \cos^2 \lambda + \frac{1}{16} \cos 2\gamma (3 - \cos 2\delta) (3 - \cos 2\lambda) \cos [2(\alpha - \phi_r - \Omega_r t)] \\
 & + \frac{1}{4} \cos 2\gamma \sin 2\lambda \sin 2\delta \cos (\alpha - \phi_r - \Omega_r t) + \frac{1}{2} \sin 2\gamma \cos \lambda \sin 2\delta \sin (\alpha - \phi_r - \Omega_r t) \\
 & + \frac{1}{4} \sin 2\gamma (3 - \cos 2\delta) \sin \lambda \sin [2(\alpha - \phi_r - \Omega_r t)], \tag{A1a}
 \end{aligned}$$

$$\begin{aligned}
 b_1(t) = & -\sin 2\gamma \cos \delta \cos \lambda \cos (\alpha - \phi_r - \Omega_r t) - \sin 2\gamma \sin \delta \sin \lambda \cos [2(\alpha - \phi_r - \Omega_r t)] \\
 & + \frac{1}{2} \cos 2\gamma \cos \delta \sin 2\lambda \sin (\alpha - \phi_r - \Omega_r t) + \frac{1}{4} \cos 2\gamma (3 - \cos 2\lambda) \sin \delta \sin [2(\alpha - \phi_r - \Omega_r t)], \tag{A1b}
 \end{aligned}$$

$$\begin{aligned}
a_{\text{II}}(t) = & \frac{1}{2} \sin \delta \cos \delta \sin \left(\gamma + \frac{\pi}{4} \right) \sin \lambda \sin (\alpha - \phi_r - \Omega_r t) - \frac{1}{4} \cos \left(\gamma + \frac{\pi}{4} \right) \cos 2\lambda \cos (\alpha - \phi_r - \Omega_r t) \sin 2\delta \\
& + \frac{1}{16} \cos \left(\gamma + \frac{\pi}{4} \right) \cos 2\delta (3 + \cos [2(\alpha - \phi_r - \Omega_r t)]) \sin 2\lambda + \frac{3}{8} \cos \left(\gamma + \frac{\pi}{4} \right) \sin 2\lambda \sin^2 (\alpha - \phi_r - \Omega_r t) \\
& - \frac{1}{8} (3 - \cos \delta) \cos \lambda \sin \left(\gamma + \frac{\pi}{4} \right) \sin [2(\alpha - \phi_r - \Omega_r t)], \tag{A1c}
\end{aligned}$$

$$\begin{aligned}
b_{\text{II}}(t) = & -\frac{1}{2} \cos \delta \cos (\alpha - \phi_r - \Omega_r t) \sin \left(\gamma + \frac{\pi}{4} \right) \sin \lambda - \frac{1}{2} \cos \delta \cos \left(\gamma + \frac{\pi}{4} \right) \cos 2\lambda \sin (\alpha - \phi_r - \Omega_r t) \\
& + \frac{1}{2} \sin \delta \cos \lambda \cos [2(\alpha - \phi_r - \Omega_r t)] \sin \left(\gamma + \frac{\pi}{4} \right) - \frac{1}{4} \sin \delta \cos \left(\gamma + \frac{\pi}{4} \right) \sin 2\lambda \sin [2(\alpha - \phi_r - \Omega_r t)], \tag{A1d}
\end{aligned}$$

$$\begin{aligned}
a_{\text{III}}(t) = & -\frac{3}{8} \cos^2 \delta \sin \left(\gamma + \frac{\pi}{4} \right) \sin 2\lambda + \frac{1}{4} \sin 2\delta \cos 2\lambda \cos (\alpha - \phi_r - \Omega_r t) \sin \left(\gamma + \frac{\pi}{4} \right) \\
& + \frac{1}{4} \sin 2\delta \sin \lambda \sin (\alpha - \phi_r - \Omega_r t) \cos \left(\gamma + \frac{\pi}{4} \right) + \frac{1}{8} (3 - \cos 2\delta) \cos \lambda \cos [2(\alpha - \phi_r - \Omega_r t)] \sin \left(\gamma + \frac{\pi}{4} \right) \sin \lambda \\
& - \frac{1}{8} (3 - \cos 2\delta) \cos \lambda \cos \left(\gamma + \frac{\pi}{4} \right) \sin [2(\alpha - \phi_r - \Omega_r t)], \tag{A1e}
\end{aligned}$$

$$\begin{aligned}
b_{\text{III}}(t) = & -\frac{1}{2} \cos \left(\gamma + \frac{\pi}{4} \right) \cos \delta \cos (\alpha - \phi_r - \Omega_r t) \sin \lambda + \frac{1}{2} \cos \delta \cos 2\lambda \sin \left(\gamma + \frac{\pi}{4} \right) \sin (\alpha - \phi_r - \Omega_r t) \\
& + \frac{1}{2} \cos \left(\gamma + \frac{\pi}{4} \right) \cos \lambda \cos [2(\alpha - \phi_r - \Omega_r t)] \sin \delta + \frac{1}{2} \cos \delta \cos 2\lambda \sin \left(\gamma + \frac{\pi}{4} \right) \sin (\alpha - \phi_r - \Omega_r t) \\
& + \frac{1}{4} \sin \left(\gamma + \frac{\pi}{4} \right) \sin \delta \sin 2\lambda \sin [2(\alpha - \phi_r - \Omega_r t)] \tag{A1f}
\end{aligned}$$

where α and δ specify the sky position of the GW sources and are called right ascension and declination, respectively. $\lambda, \gamma, \Omega_r$, and ϕ_r are the latitude of the antenna position, the angle between the local East direction and the bisector of the antenna, the angular speed of the Earth, and the initial phase which defines the antenna position on the Earth at $t = 0$, respectively.

-
- [1] M. Ando, K. Ishidoshiro, K. Yamamoto, K. Yagi, W. Kokuyama, K. Tsubono, and A. Takamori, *Phys. Rev. Lett.* **105**, 161101 (2010).
- [2] K. Ishidoshiro, M. Ando, A. Takamori, H. Takahashi, K. Okada, N. Matsumoto, W. Kokuyama, N. Kanda, Y. Aso, and K. Tsubono, *Phys. Rev. Lett.* **106**, 161101 (2011).
- [3] A. Shoda, M. Ando, K. Ishidoshiro, K. Okada, W. Kokuyama, Y. Aso, and K. Tsubono, *Phys. Rev. D* **89**, 027101 (2014).
- [4] K. Nakamura and M. Ando, *Phys. Rev. D* **90**, 064008 (2014).
- [5] B. Abbott *et al.* (LIGO Scientific Collaboration), *Rep. Prog. Phys.* **72**, 076901 (2009).
- [6] T. Accadia *et al.* (VIRGO Collaboration), *JINST* **7**, P03012 (2012).
- [7] Y. Aso, Y. Michimura, K. Somiya, M. Ando, O. Miyakawa, T. Sekiguchi, D. Tatsumi, and H. Yamamoto (KAGRA Collaboration), *Phys. Rev. D* **88**, 043007 (2013).
- [8] P. Amaro-Seoane, S. Aoudia, S. Babak, P. Binetruy, E. Berti *et al.*, *Classical Quantum Gravity* **29**, 124016 (2012).
- [9] S. Kawamura, M. Ando, N. Seto, S. Sato, T. Nakamura *et al.*, *Classical Quantum Gravity* **28**, 094011 (2011).
- [10] E. J. Colbert and R. F. Mushotzky, *Astrophys. J.* **519**, 89 (1999).
- [11] S. Farrell, N. Webb, D. Barret, O. Godet, and J. Rodrigues, *Nature (London)* **460**, 73 (2009).
- [12] D. R. Pasham, T. E. Strohmayer, and R. F. Mushotzky, *Nature (London)* **513**, 74 (2014).
- [13] H. Baumgardt, J. Makino, and P. Hut, *Astrophys. J.* **620**, 238 (2005).
- [14] K. Gebhardt, R. M. Rich, and L. C. Ho, *Astrophys. J.* **634**, 1093 (2005).
- [15] M. C. Miller, *Classical Quantum Gravity* **26**, 094031 (2009).

- [16] H. Hirakawa, K. Narihara, and M. Fujimoto, *J. Phys. Soc. Jpn.* **41**, 1093 (1976).
- [17] S. Bonazzola and E. Gourgoulhon, *Astron. Astrophys.* **312**, 675 (1996).
- [18] P. Jaranowski, A. Krolak, and B. F. Schutz, *Phys. Rev. D* **58**, 063001 (1998).
- [19] B. F. Schutz, *Classical Quantum Gravity* **28**, 125023 (2011).
- [20] L. S. Finn, *Phys. Rev. D* **46**, 5236 (1992).
- [21] C. Cutler and E. E. Flanagan, *Phys. Rev. D* **49**, 2658 (1994).
- [22] P. Jaranowski and A. Krolak, *Living Rev. Relativity* **8**, 3 (2005).
- [23] P. R. Saulson, *Phys. Rev. D* **30**, 732 (1984).
- [24] S. A. Hughes and K. S. Thorne, *Phys. Rev. D* **58**, 122002 (1998).
- [25] K. S. Thorne and C. J. Winstein, *Phys. Rev. D* **60**, 082001 (1999).
- [26] J. Harms, B. J. J. Slagmolen, R. X. Adhikari, M. C. Miller, M. Evans, Y. Chen, H. Müller, and M. Ando, *Phys. Rev. D* **88**, 122003 (2013).
- [27] J. C. Driggers, J. Harms, and R. X. Adhikari, *Phys. Rev. D* **86**, 102001 (2012).
- [28] M. Maggiore, *Gravitational Waves: Volume 1: Theory and Experiments* (Oxford University Press, New York, 2007).
- [29] C. Cutler, *Phys. Rev. D* **57**, 7089 (1998).
- [30] R. Takahashi and N. Seto, *Astrophys. J.* **575**, 1030 (2002).
- [31] B. F. Schutz, [arXiv:gr-qc/0111095](https://arxiv.org/abs/gr-qc/0111095).
- [32] Y. Guersel and M. Tinto, *Phys. Rev. D* **40**, 3884 (1989).
- [33] L. Wen and Y. Chen, *Phys. Rev. D* **81**, 082001 (2010).
- [34] N. Yunes and X. Siemens, *Living Rev. Relativity* **16**, 9 (2013).
- [35] J. Harms, J.-P. Ampuero, M. Barsuglia, E. Chassande-Mottin, J.-P. Montagner, S. N. Somala, and B. F. Whiting (to be published).